Observations on cohesive bed reworking by waves: Atchafalaya Shelf, Louisiana

Cihan Sahin,[1] Ilgar Safak,[2] Alexandru Sheremet,[1] and Ashish J. Mehta[1]

Received 10 December 2011; revised 28 July 2012; accepted 8 August 2012; published 20 September 2012.

[1] Wave, current, acoustic backscatter and suspended sediment concentration measurements (both single-point and vertical profiles estimated by conversion of acoustic backscatter data) are used to investigate wave-current-cohesive sediment interaction on the muddy Atchafalaya inner shelf. During an energetic storm, we propose that bed state follows a cycle of dilation due to fluidization, erosion, deposition with fluid mud formation and consolidation. A one-dimensional-vertical cohesive sediment transport model is calibrated using current and concentration profiles to estimate the physical parameters that could not be measured directly, e.g., bottom stresses. Estimated bed position and computed bottom stresses suggest that the critical erosion threshold is in the range of 0.3 Pa to 0.5 Pa. The study site is impacted by a sediment-laden fresh water plume coming from the Atchafalaya River mouth. Bed density evolution during the storm is estimated from vertical sediment exchange between the water column and the bed excluding the duration of passage of a sediment-carrying water front. The values are in the range of 1,030 kg/m^3 to 1,200 kg/m^3 and indicate that the bed density increases during the erosion phase and decreases during deposition. At the end of the storm, it shows a steady increasing trend during hindered settling and exceeds the space-filling value during consolidation. Both the critical erosion shear stress and bed density values are consistent with the results of laboratory tests on samples from the experimental site.

Citation: Sahin, C., I. Safak, A. Sheremet, and A. J. Mehta (2012), Observations on cohesive bed reworking by waves: Atchafalaya Shelf, Louisiana, *J. Geophys. Res.*, *117*, C09025, doi:10.1029/2011JC007821.

1. Introduction

[2] Numerous studies of muddy coasts (e.g., southwest coast of India and East Coast of China [*Jiang and Mehta*, 1996, 2000]; the Amazon Delta [*Cacchione et al.*, 1995]; Eel River in Northern California, and the Po Delta [*Traykovski et al.*, 2000, 2007]; Atchafalaya Shelf, Gulf of Mexico [*Allison et al.*, 2000]) suggest that a strong coupling exists between hydrodynamics and cohesive bed dynamics. Bottom stresses induced by energetic waves can result in bulk stresses that exceed the yield threshold and rework the bed sediment through a combination of processes such as bed liquefaction, fluidization (swelling due to mixing with water), erosion, and deposition. Under hindered-settling conditions, a dense and viscous layer of fluid mud can form in the vicinity of the bed, and induce substantial wave energy dissipation [*Jiang and Mehta*, 1996; *Sheremet and Stone*, 2003; *Allison et al.*, 2005; *Sheremet et al.*, 2005; *Winterwerp et al.*, 2007; *Sheremet et al.*, 2011].

[1]Department of Civil and Coastal Engineering, University of Florida, Gainesville, Florida, USA.
[2]Department of Environmental Sciences, University of Virginia, Charlottesville, Virginia, USA.

Corresponding author: C. Sahin, Department of Civil and Coastal Engineering, University of Florida, Weil Hall 365, Gainesville, FL 32611, USA. (cisahin@ufl.edu)

0148-0227/12/2011JC007821

[3] The most common description of the state of the cohesive bed used in wave-sediment interaction studies, i.e., Newtonian viscous-fluid [e.g., *Gade*, 1958; *Dalrymple and Liu*, 1978; *Ng*, 2000], has been criticized for over-estimating mud viscosity [*Maa and Mehta*, 1990]. Alternative models proposed to correct this, such as single- or multilayered visco-elastic models [*Hsiao and Shemdin*, 1980; *Maa and Mehta*, 1990; *Foda et al.*, 1993], or visco-plastic ones [*Liu and Mei*, 1989, 1993; *Chan and Liu*, 2009], are assumed to provide a physical description closer to the field reality. Visco-elastic models can account for both liquid and elastic phases of mud; visco-plastic models provide a better representation of high-density mud phases during the incipient stages of bed reworking. These formulations (and perhaps others) can be justified theoretically (see for example, the systemic discussion in *Jain and Mehta* [2009]). However, supportive observational data remain scarce. One reason is the considerable difficulty in observing directly and continuously the evolution of bed-sediment state during interesting events (storms). Another is the fact that methodologies for in-situ observations of coupled hydrodynamics and sediment-transport processes are far from mature.

[4] The observations discussed here were made on the muddy inner shelf fronting the Atchafalaya Bay along the Gulf of Mexico coast of Louisiana, USA, between February and April 2008. The muddy Atchafalaya subaqueous clinoform (water depth <8 m extending tens of kilometers offshore) and

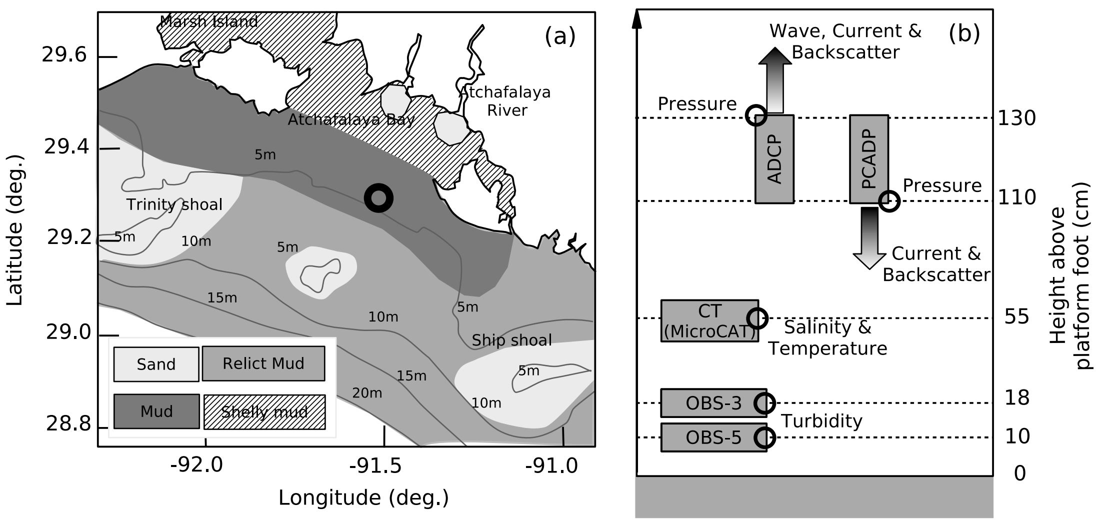

Figure 1. (a) Distribution of the surficial sediments in the Atchafalaya region of the Louisiana coast (Gulf of Mexico). The circle marks the location (29.26° latitude North, 91.57° longitude West) of the instrument platform. (b) The positions of the instruments deployed with respect to the bed. For point measurements, the location of the sampling volume is marked by a circle. For profilers, arrow indicates the direction of acoustic signal.

the adjacent chenier plains have been the focus of several previous studies [*Allison et al.*, 2000; *Sheremet and Stone*, 2003; *Allison et al.*, 2005; *Sheremet et al.*, 2005; *Draut et al.*, 2005; *Kineke et al.*, 2006; *Jaramillo et al.*, 2009; *Safak et al.*, 2010]. In summary, between December and April the wave climate on the shelf is dominated by quasiperiodic pulses of energetic wave activity (wave heights >1 m) associated with cold atmospheric fronts that sweep over the region moving eastward. Over the shallow Atchafalaya inner shelf, waves rework the bed and mobilize bed sediment. At the same time, rain associated with atmospheric fronts also increases the Atchafalaya River discharge, releasing large quantities of sediment that is then advected over the shelf by tidal currents. High-concentration, near-bed fluid-mud layers have been observed to form and move onshore or offshore over the clinoform, driven by gravity and supported by wave-induced stresses [e.g., *Kineke et al.*, 2006; *Jaramillo et al.*, 2009]. Two competing processes are assumed to generate these flows: advection of sediment by the plume of the Atchafalaya River; and local, wave-induced bed reworking. The relation between these two mechanisms is not well understood.

[5] Field experiments on the Atchafalaya Shelf [e.g., *Kineke et al.*, 2006; *Jaramillo et al.*, 2009; *Safak et al.*, 2010; *Sheremet et al.*, 2011] monitored flow and sediment mainly using optical sensors calibrated for estimating the local suspended sediment concentration (SSC), and acoustic sensors mainly for recording the flow velocity (as single point measurements or vertical profiles). Optical sensors provide a few SSC measurement points that are in general not dense enough for a satisfactory characterization of the sediment content in the water column. In sandy environments, the acoustic backscatter intensity data are routinely used to estimate the vertical SSC structure [*Lynch et al.*, 1991; *Thorne et al.*, 1993; *Thosteson and Hanes*, 1998; *Thorne and Hanes*, 2002]. In muddy environments the conversion of acoustic backscatter information to SSC profile is more complicated; e.g., important sediment characteristics such as particle shape, density, and settling velocity, which depend on the flow characteristics and the amount of sediment in suspension. Most of the studies in such environments [e.g., *Gartner*, 2004; *Hoitink and Hoekstra*, 2005] focused on the performance of acoustic profilers in dilute cohesive sediment suspensions (concentrations on the order of 0.1 kg/m^3). C. Sahin et al. (Observations of sediment stratification on the muddy Atchafalaya Shelf, Louisiana, USA, submitted to *Marine Geology*, 2012) suggest that the methodology can be extended to include cohesive sediments, and used with virtually any acoustic profiler in relatively high concentration (up to the order of 10 kg/m^3) environments.

[6] This paper represents an effort to assemble the observations of flow velocities, SSC values (single-point measurements, as well as vertical profiles obtained through the conversion of acoustic backscatter), and seabed position – into a reconstructed description of wave-current-sediment interaction on the Atchafalaya inner shelf. Observed sediment concentrations and flows are used to calibrate a one-dimensional-vertical (1DV) sediment transport model [*Hsu et al.*, 2009], which in turn is used to estimate physical parameters that could not be measured directly, such as the turbulent bottom stresses. Sediment characteristic parameters (e.g., yield stress and bulk density) obtained from previous laboratory tests on samples from the experimental site [*Robillard*, 2009] are used to validate the findings (e.g., critical shear stress for erosion, bed density at the onset of erosion). The implications of the results are discussed in relation to bed response to hydrodynamic forcing and the importance of sediment resuspension relative to advection.

2. Field Experiment

2.1. Site and Instrumentation

[7] The observations were made in Spring 2008 on the muddy inner shelf fronting the Atchafalaya Bay (Figure 1a),

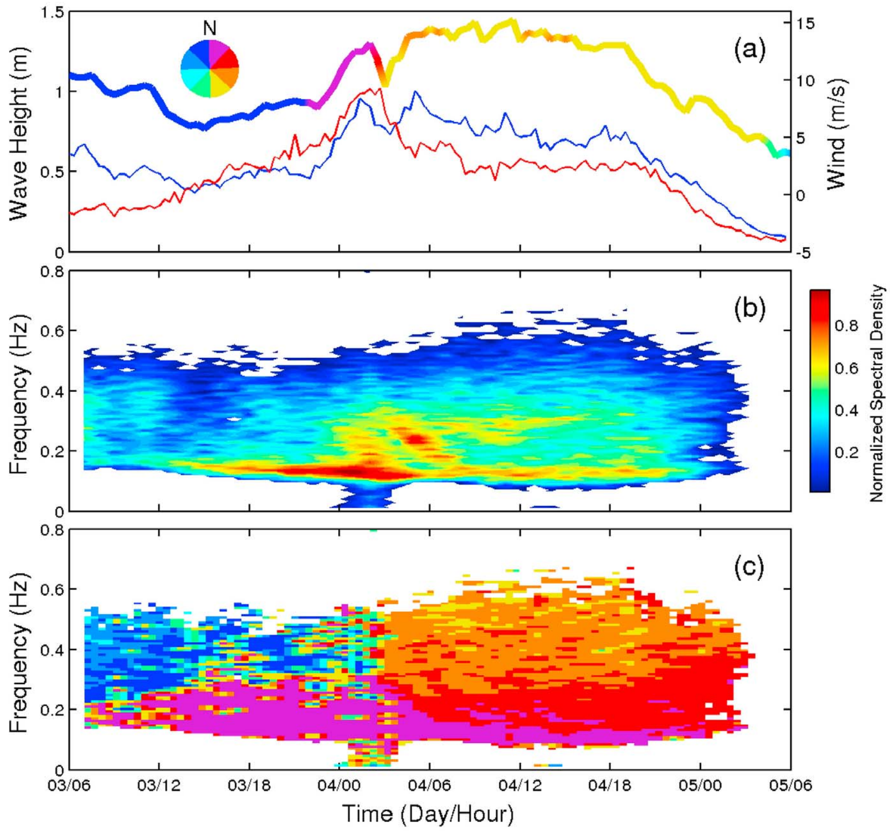

Figure 2. Evolution of wave frequency spectrum and propagation direction during the storm of March 3rd to 5th, 2008. (a) Wind speed and direction (color-coded), and significant wave height in the short-wave (f >0.2 Hz, blue) and swell ($f \leq 0.2$ Hz, red) bands. (b) Normalized spectral density. (c) Peak direction of each spectral band. In the direction convention used, N means flowing (or propagating) northward.

near the 4-m isobath. The location of the instrumented platform (Figure 1b) coincides with that of the 2006 measurements (platform "T2A" in *Jaramillo et al.* [2009] and "2006 experiment" in *Safak et al.* [2010]). It is assumed here that the sediment properties required for numerical simulations (e.g., floc size range, fractal dimension, see values in section 3.2) were practically the same in the two experiments.

[8] The vertical structure of the flow velocity in the first mab (meter above the bed) was observed using a PC-ADP (Pulse-Coherent Acoustic Doppler Profiler, Sontek/YSI), that sampled at 2-Hz continuously in 27 bins of 3.2 cm with a 30-cm blanking distance. Direct SSC observations were provided by an OBS-5 (Optical Backscatterance Sensors, D&A Instruments, Campbell Sci.) that recorded 2-min averages of turbidity, and an OBS-3 (D&A Instruments, Campbell Sci.) sampling synchronously with the PC-ADP. Upper water column currents and surface waves were observed using a 1200-kHz, ADCP (Acoustic Doppler Current Profiler, Teledyne RD Instruments). Current profiles were sampled at 0.7 Hz and recorded as 10-min averages in 20-cm vertical bins, with the lowest bin centered at about 2-m above the bed. A Seabird MicroCAT at 55 cmab sampled salinity and temperature synchronously with the PC-ADP.

[9] Directional wave spectra were estimated from measurements of pressure, acoustic surface tracking, and velocity profiles, sampled at 2 Hz in 40-min measurement bursts per hour. Wave data were processed using the processing packages WavesMon and WaveView (Teledyne RD Instruments), and from these directional spectra were produced at 127 frequencies with a frequency resolution of 0.0078 Hz and angular resolution of 4 degrees. The significant wave height was estimated by using the relation $H^2 = 16 \int S(f)df$ where S is the power spectral density of sea surface elevation at frequency f. A HOBO micro-station (Onset, Inc.) located 7-m above the sea surface provided 30-min averages of wind speed and direction.

2.2. Observations

[10] The March 3–5, 2008 (time reported in this study is UTM) period discussed here spans the duration of an atmospheric cold front that passed over the experimental site on March 4th with southerly winds changing abruptly to northerly (Figures 2a and 2c). The event was preceded by a week of relatively calm conditions (4-s waves rarely exceeding 0.5 m). The front produced wave heights reaching 1.3 m, with 1-m height swells that propagated consistently northward through March 4th, despite the shift in wind direction. As winds weakened to about 5 m/s, rapid decay in wave activity over all frequency bands reduced the significant height from approximately 0.9-m height to 0.1-m in six hours. This phenomenon was observed before and shown to be related with wave dissipation induced by the muddy bed [*Sheremet and Stone*,

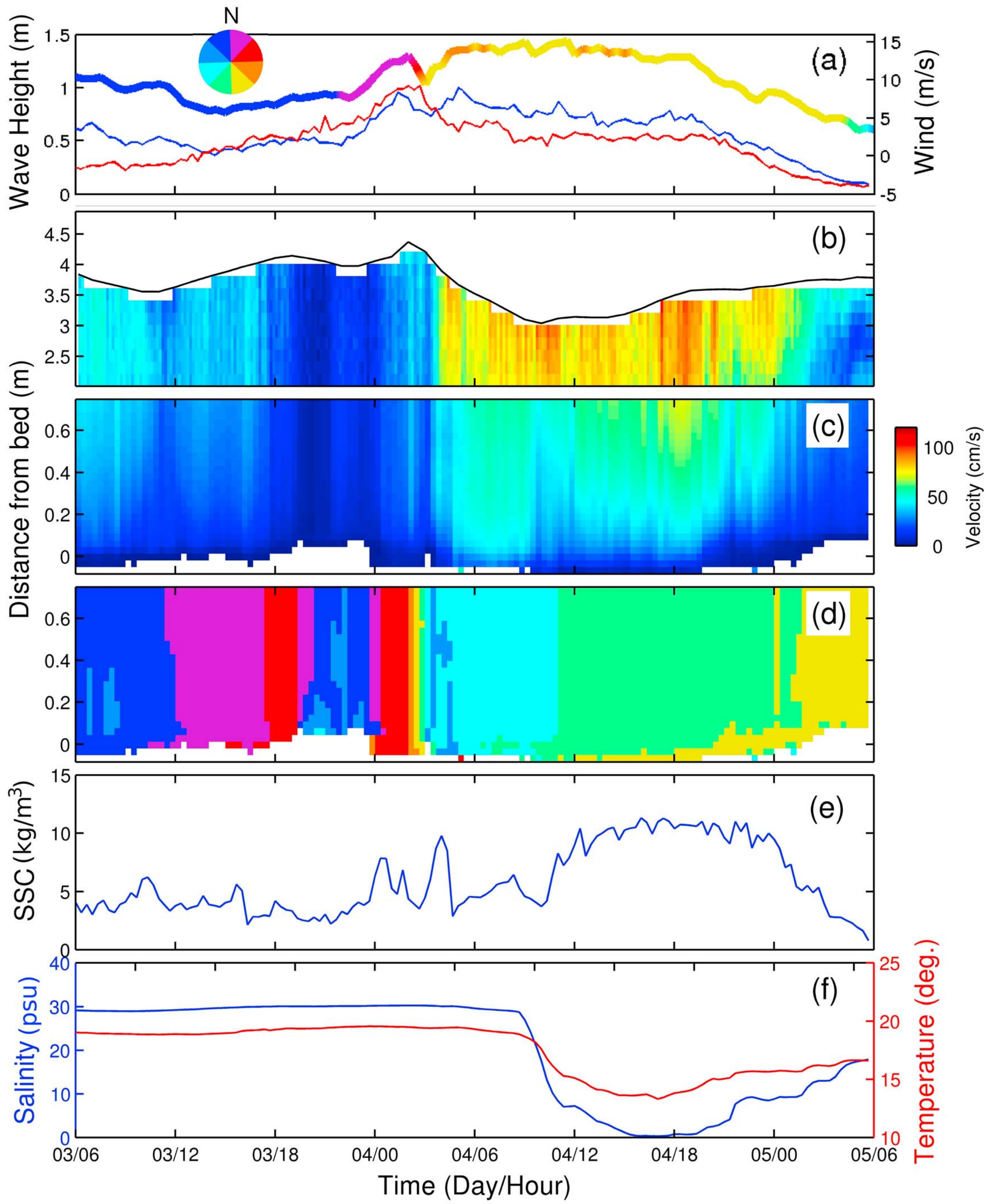

Figure 3. Storm of March 3rd to 5th, 2008: (a) Wind speed and direction and significant wave heights (short-wave: blue and swell: red). Vertical structure of mean current recorded by the (b) ADCP and (c) PC-ADP. (d) Direction of PC-ADP mean currents. (e) SSC observed by the OBS-3 located at 18 cmab. (f) Salinity (blue) and temperature (red) at 55 cmab. Locations of the instruments are shown in Figure 1b.

2003; *Sheremet et al.*, 2005; *Jaramillo et al.*, 2009; *Sheremet et al.*, 2011].

[11] The strongest currents coincided with the wind shifting direction on March 4th (Figure 3). Two current pulses can be identified in the PC-ADP observations (Figures 3c and 3d). The first pulse flowing toward WSW was observed on March 4th from 4:00 to 10:00 hours, associated with a 1-m drop in the mean water level (Figure 3b). This pulse is likely related to the flushing of the storm surge produced by the atmospheric cold front and the change in the wind direction after frontal passage.

[12] A second, stronger pulse flowing toward SSW followed (March 4th 12:00 to March 5th 00:00 hours), associated with an increase in the surface elevation and a return to the normal tidal cycle. This pulse transported fresh, sediment-laden water likely associated with the Atchafalaya

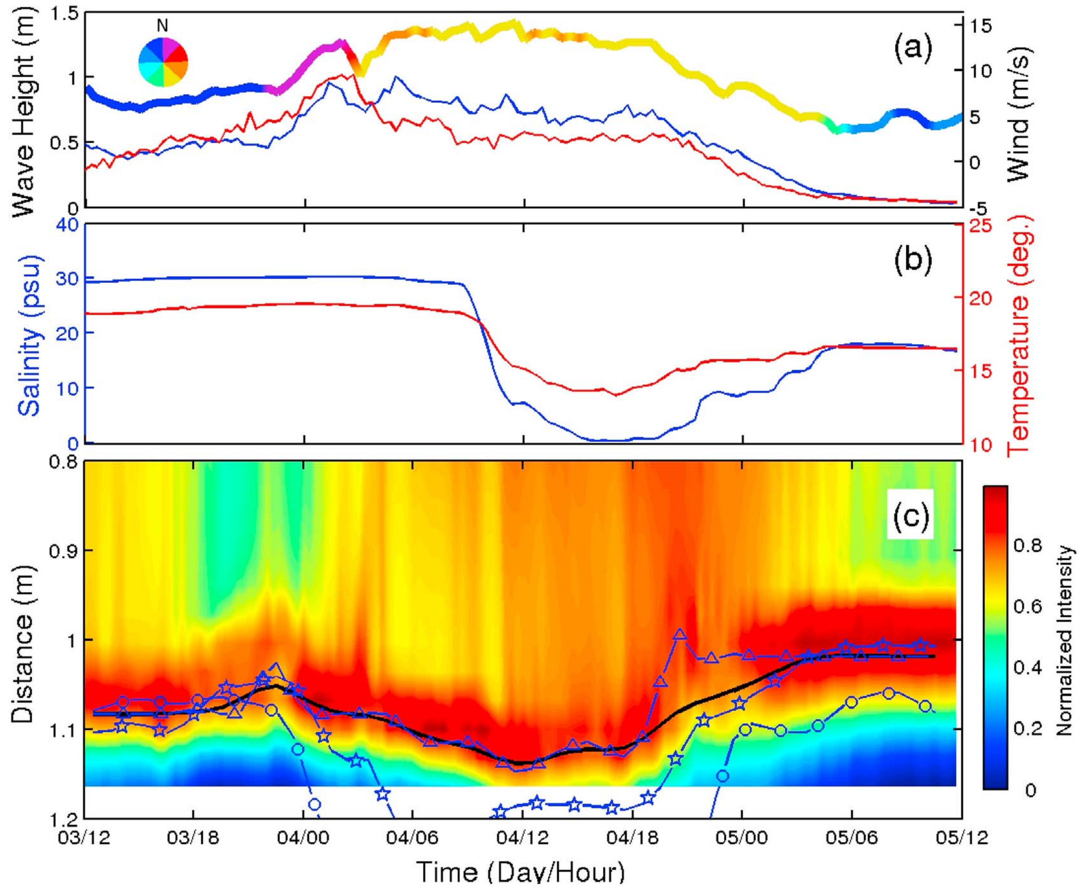

Figure 4. Evolution of bed position indicators and state during the storm of March 3rd to 5th, 2008. (a) Wind speed and direction (color-coded thick line), and significant wave heights (short-wave: blue and swell: red). (b) Salinity (blue) and temperature (red) at 55 cmab (same as in Figure 3f). (c) Normalized PC-ADP acoustic backscatter intensity. The lines represent locations of: maximum backscatter intensity (triangles), zero mean horizontal velocity (stars), and zero RMS horizontal velocity (circles). The smoothed estimate of the bed position is marked by the continuous thick line.

River plume (salinity less than 5 psu, water temperature 13°C, and a significant increase in SSC) that displaced seawater (30 psu salinity, temperature 18°C, SSC approximately 4 kg/m^3; Figures 3e and 3f). The water front resulting from the colliding masses passed over the experimental site within approximately three hours, illustrated by the rapid drop in salinity and temperature (Figure 3f); SSC values show weaker variation with perhaps an increase by a factor of 2. Starting from March 4th 18:00 hours wave activity decayed and sediment settling and advection cleared the water column rapidly, with SSC values decreasing from $\sim$10 kg/m^3 to almost nil in six hours (Figure 3e).

[13] The current velocity profile can be used in conjunction with the PC-ADP acoustic backscatter observations (Figure 4) to assess the dynamic behavior of the seabed. Because strong reflections are typically associated with sharp density gradients, the position of the interface is estimated here as the smoothed position of the near-bed local backscatter maximum. This definition includes sharp lutoclines of high-density fluid-mud layers (e.g., March 5th, Figure 4c), but excludes weak maxima (e.g., March 4th 21:00), when the bed cannot be reliably identified. The elevations of zero-mean velocity (ZMV) and zero-RMS velocity (ZRV) can be used to investigate the depth of penetration of steady current (hydrodynamic depth) and oscillatory motions (wave penetration depth), respectively [e.g., *Jaramillo et al.*, 2009]. The results, shown in Figure 4c, are informative.

[14] At noon on March 3rd, the bed position coincides with ZMV and ZRV, suggesting a solid bed. As swell activity increases, the vertically stretchable bed level rises suggesting a bed dilation due to water pumping into the bed (March 3th 18:00 to March 3th 22:00 hours). This is consistent with the water entrainment by the fluid mud layer during which water flux occurs from the upper fluid into the moving lower fluid mud layer with the results that fluid mud is diluted and sediment-water interface rises [*Winterwerp and van Kesteren*, 2004]. This implies that prior to dilation the “solid” bed would be more appropriately described as a “stationary soft” bed due to previous recent storms, an ephemeral state without horizontal movement. Following dilation, the bed level falls continuously for about 14-hours (erosion, March 3th 22:00

to 12:00 hours). Bed accretion begins on March 4th at 12:00 hours and continues until early morning of March 5th.

[15] With dilation ZRV separates and dips rapidly beyond the range of the instrument, suggesting that dilation of the bed is accompanied by increased penetration of wave oscillatory motion. Soon (1–2 hours) after bed dilation, ZMV also separates and dips. The three curves diverge during the erosion phase (morning of March 4th) involving the entrainment of fluid mud as well as the erosion of any solid bed below fluid mud. Both processes collectively manifest as an erosion flux. The ZMV and ZRV curves begin to converge slowly at the onset of bed accretion due to the flux of depositing sediment.

[16] Throughout March 4th an approximately 6-cm surficial bed layer appears to have non-zero mean velocity (order of 5 cm/s, Appendix A); a thicker surficial layer oscillates with the waves. At the end of the storm, ZMV and the bed positions overlap again, with ZRV approximately 5-cm lower. This behavior is consistent with the formation of a layer of hindered-settling mud with an initial thickness (March 4th 10:00 hours) of possibly 20–30 cm. The position of the bed at the end of the storm cycle is approximately 7–8 cm higher than at the onset. A comparison with water levels recorded at nearby stations showed that the instrument platform did not sink (water level differences were consistently less than 3 cm), which suggests that the rise in the bed elevation was due to deposition.

[17] This interpretation of the bed evolution is consistent with the observed hydrodynamics. As mentioned before, under low wave energy and current speed (afternoon March 3rd, Figure 3) the bed is stationary soft mud; it dilates with increasing wave energy and erodes continuously thereafter through noon, March 4th. The deposition (accretion) phase coincides with a decrease in wave activity. In the afternoon of March 4th, with the arrival of a second current pulse carrying fresh, sediment-laden water (Figures 3 and 4), SSC increases to 10 kg/m^3 and remains approximately constant until early morning of March 5th. At the end of the storm, the persistence of oscillations in the 5-cm thick surficial layer suggests the formation of a fluid mud layer due to hindered settling.

[18] In summary, we **propose** the following bed reworking cycle by waves and currents going through stages that appear to be consistent with: 1) dilation due to fluidization; 2) erosion, possibly shearing of surficial layers; 3) deposition (accretion) with fluid-mud formation; and 4) consolidation with increasing bed density due to de-watering. In this sequence, both local (erosion, deposition) and non-local (advective sediment flux convergence) processes appear to play noteworthy roles.

3. Reconstruction of Water Column Processes

3.1. Conversion of Acoustic Backscatter to SSC Profile

[19] The vertical SSC profiles were estimated from the intensity of the acoustic backscatter profiles of the PC-ADP [e.g., *Sahin et al.*, 2011]. The conversion algorithm assumes a floc size independent of depth and applies a method developed for sand [*Sheng and Hay*, 1988; *Thorne et al.*, 1993; *Thorne and Hanes*, 2002] in two steps: a) a procedure for estimating the PC-ADP system constant k_t, and b) an optimization search for a depth-independent, "effective" floc size, corresponding to the best fit between acoustic backscatter and optical SSC estimates. Briefly, the vertical profile of SSC is calculated as follows:

$$SSC = \left\{ \frac{V(r) r \psi}{k_s k_t} \right\}^2 e^{4r\alpha}, \tag{1}$$

$$k_s = \frac{\langle f_f \rangle}{\sqrt{\langle a \rangle \rho}}, \tag{2}$$

where $V(r)$ is the backscattered signal from the slant range r along the axis to the ensonified volume, ψ is the near-field correction factor describing the departure from spherical spreading in the near-field of the transducer, k_s embodies the scattering properties of sediment, α is the acoustic absorption coefficient, f_f is a form function for the scattering characteristics of suspended particles, a is the mean radius of sediment in suspension and ρ denotes sediment density (density of mud flocs in this case). The angular brackets indicate mean value over the particle-size distribution. The execution of the algorithm will be described in detail elsewhere (Sahin et al., submitted manuscript, 2012). The instrument constant k_t was determined using an optimization approach that sought the value of k_t that reproduced the optical SSC observations best.

[20] The PC-ADP backscatter was calibrated for the instrument constant k_t using independent OBS measurements made between February 22nd and March 3rd at two heights above the bed (the OBS-5 stopped functioning after March 3rd). Because SSC values were low (order of 1–2 kg/m^3; not shown) during that period, and no floc size observations could be made, the procedure used a constant floc diameter D_f = 200 μm. This is acceptable because in previous applications [e.g., *Sahin et al.*, 2011], the system constant k_t did not show sensitivity to floc size. This is also consistent with previous studies at the site [*Safak et al.*, 2010], that indicated a variability range for D_f between 100 μm and 350 μm with an average value of around 200 μm.

[21] For the March 3rd to March 5th period the search range for the effective floc size was between 50 μm and 350 μm. The SSC profile and the floc size for each burst over the duration of the experiment including the major event of interest between March 3rd–5th were determined. The deviation (RMS error) between the calculated concentrations and the optical measurements was 0.37 kg/m^3 with correlation coefficient r^2 = 0.92.

3.2. Numerical Simulations

[22] Numerical simulations are based on the 1DV boundary-layer model for cohesive beds developed by *Hsu et al.* [2009]. The vertical structures of turbulent flow parameters and suspended sediment concentration are calculated by calibrating the model with measurements of waves and currents, and estimates of concentration. The model accounts for combined wave-current flow and integrates the two-phase (fluid-sediment) Reynolds-averaged equations based on a $k-\epsilon$ closure. The momentum balance is between free-stream horizontal pressure gradient (prescribed as flow forcing due to waves and currents) and momentum transport by fluid shear stresses (both viscous and turbulent). The sediment concentration is balanced between gravitational settling and turbulent mass flux. The effect of sediment on fluid turbulence is accounted for in the turbulence balances by the density-

induced stratification due to vertical gradient of suspended sediment concentration. The sediment phase is defined in the model with a primary particle size (D_p), D_f and fractal dimension (n_f), all of which are independent of location above the bed and time (constant floc density and settling velocity). Settling velocity is modeled using the Stokes law with hindered settling effect incorporated. The standard simulation procedure starts the model from an initial rest state with zero SSC profile and seeks a steady state matching the observed mean flow structure and SSC profile. The calculations were made with the relaxation time method that generates a current profile with a user-defined depth-averaged velocity. Based on the spectra of the velocity measurements, the oscillatory part of the flow was described using a representative wave with period corresponding to the spectral peak frequency and amplitude that yields a signal with a standard deviation equal to the one obtained from the measurements.

[23] Sediment is made available to the simulation domain at the lower boundary. The bottom boundary is set at a level close to actual mobile bed. A highly concentrated fluid layer between this layer and actual mobile bed is neglected. Sediment availability is controlled through critical shear stress near the bed (τ_c) and the resuspension coefficient (γ_o). The former is site specific and no characterization for it is available for the study site. The latter usually varies by two orders of magnitude [*Hsu et al.*, 2007]. In the previous applications, vertical structures of sediment concentration calculated in numerical experiments with several ($\tau_c - \gamma_o$) pairs did not indicate a sensitivity on τ_c [*Safak et al.*, 2010; *Hsu et al.*, 2009]. Also, the effect of varying τ_c can be compensated by varying resuspension coefficient to match the water column data [*Hsu et al.*, 2007]. Therefore τ_c = 0.4 Pa, which is within the range of 0.05–1.1 Pa suggested by *Hsu et al.* [2007] and used by *Safak et al.* [2010] in the same area, was used. The resuspension coefficient [e.g., *Hsu et al.*, 2007, equation (20)] was used as a free parameter to control sediment erosion. The calibration parameters in numerical simulations were D_f and γ_o.

[24] The simulation domain was defined to span the bottom meter above bed, with the bed position (Figure 4c) as the bottom boundary, the upper boundary at approximately 22 cm above the topmost PC-ADP bin, and a vertical resolution of 3.2 cm equal to the PC-ADP bin height. In preliminary test runs, the model did not show sensitivity to grid size as the current-boundary layer dominated the process, and was well resolved at the 3.2-cm grid size. The floc size was varied between 50 μm and 350 μm (density between 1,100 kg/m^3 and 1,350 kg/m^3). In all the simulations the resuspension coefficient was smaller than 10^{-2}, consistent with previous estimates [*Hsu et al.*, 2007, 2009; *Safak et al.*, 2010].

[25] The model has been used as an investigative tool: if it can be tuned to reproduce the observations, its inner balance could be used to draw inferences concerning the non-observable physics. However, in its present implementation the model cannot be expected to fully reproduce observations made under non-stationary conditions. Two examples of such conditions are the time segment with bed dilation from March 3rd, 18:00 to 24:00 hours, and arrival of the sediment-laden water front on March 4th from 12:00 to 18:00 hours.

[26] The former non-stationary condition is simply a calm event, with a weak flow velocity (order of 1 cm/s, Figures 3b–3d). The model is unable to produce the turbulence required to sustain the observed low SSC values (Figures 4c and 5b), and the stationary solution predicts almost the entire sediment mass settled on the bed. In order to simulate this period accurately, the model would need to reproduce the non-stationary conditions such as dilation of the bed and associated changes in erosion processes, both of which are interesting but beyond the scope of this paper. The latter event is more challenging because some sediment likely enters the system through advection that is unsupportive of the model assumption of vertical sediment balance with a bottom boundary sediment source. The frontal passage (starting with the wind direction change on March 4th, Figure 5a) is equivalent to a sudden emergence of a sediment source high in the water column. During this period, even if the numerical simulations are not obviously wrong, the simulations should be treated with caution as the model likely over-estimates the bottom stresses such that the increase in the SSC due to sediment advection is compensated with increasing bottom stress.

[27] However, the remarkable spatial uniformity at the experimental site (e.g., bottom slopes less than 0.001 over tens of km) suggests that sediment flux convergence may be negligible, i.e., the horizontal gradients are small in general, which justifies use of a 1-D approach, with the possible exception of water fronts produced by the Atchafalaya River plume. The relatively stable mean SSC, temperature and salinity values before and after the passage of the water front on March 4th 12:00 hours (Figure 3) supports the inference that significant sediment-flux convergence events are short-lived (order of hours) but widely distributed when they occur.

[28] Based on these considerations, the model was applied over the entire storm duration. The calibration was made with different $D_f - \gamma_0$ pairs to find the one that gives best agreement (in a least square sense throughout the model domain) with current velocity and SSC profiles. Overall, the numerical reconstruction of the SSC vertical structures agree well with the estimated values (Figures 5b and 5c). Normalized RMS error range was between 4 and 60% (18% average). The model also captured the vertical structure of the flow well with normalized RMS error range of 6 to 56% (23% average). The errors were less than 10% for most of the simulated period, the simulations with large errors mostly correspond to the period of bed dilation. The simulations can be expected to be valid for the entire duration, with the possible exclusion of the weakly non-stationary bed dilation segment on March 3rd 18:00 hours, and water-front passage around March 4th 12:00 hours.

4. Results

4.1. Critical Shear Stress for Erosion

[29] Surface erosion occurs when layers of sediment are eroded and mobilized if the critical shear stress for erosion is exceeded by stresses induced by waves and currents. However, sediment resuspension can be observed when stresses are lower then the critical shear stress (e.g., between March 4th 00:00–03:00 hours in Figure 5). This should be attributed to entrainment which occurs in case of fluid mud when non-turbulent mud layer is entrained by the upper turbulent water layer [*Winterwerp and van Kesteren*, 2004].

[30] The evolution of the observed bed position (e.g., Figures 4c, 5b and 5c) and the bottom stress calculated by the model (average over one wave period when the steady state

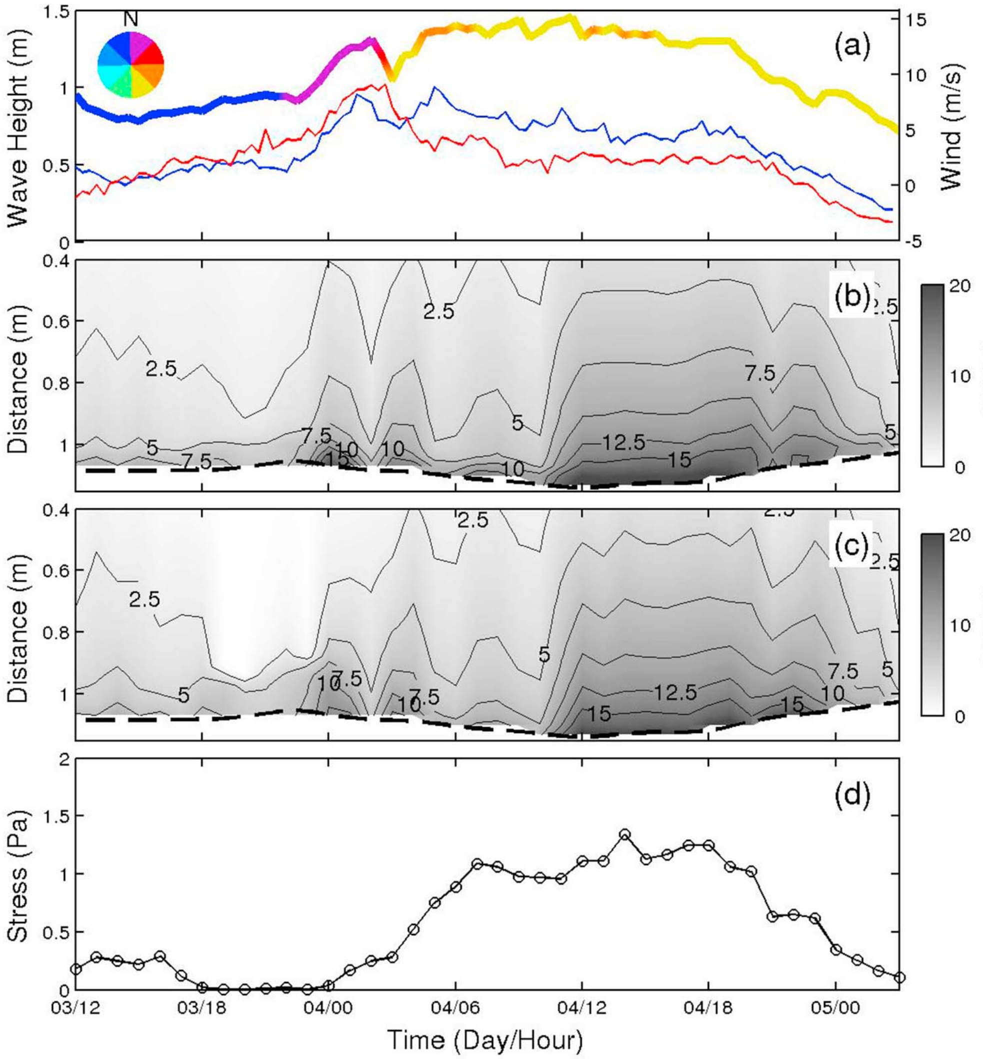

Figure 5. Model simulations for the storm of March 3rd–5th, 2008. (a) Wind speed and direction, and significant wave heights (short-wave: blue and swell: red). (b) SSC vertical structure estimated from PC-ADP backscatter. (c) Numerically-simulated SSC vertical structure. (d) Turbulent Reynolds stress at bed level (defined as the continuous line in Figure 4b).

solution is reached) in the vicinity of the bed (Figure 5d) are consistent, despite being dynamically unconnected (in the model, the bed level is prescribed and does not evolve during simulation). During the low currents and wave activity period before March 4th, shear stress values are less than 0.3 Pa with an average of 0.22 Pa. Stress values begin to increase around midnight March 4th with the increase of wave activity. Between March 4th 00:00–03:00 hours, bottom stress is still less than 0.3 Pa and the amount of sediment in the water column increases suggesting the entrainment of soft layers of bed occurs. During this period, the numerical model captures the observed flow and sediment structures with increased resuspension coefficient. The layers of initially consolidated sediment are eroded when the bottom stress increases from 0.3 Pa to 0.5 Pa after March 4th 03:00 hours. The model maintains the bottom stress at about 1.2 Pa for approximately 12 hours around the arrival of the sediment-laden freshwater front on March 4th 12:00 hours, then begins to decrease the stress steadily, consistent both with the decrease in current and wave activity.

[31] Using an experimental relation proposed by *Migniot* [1968], the upper Bingham yield stress τ_y (stress determined by extrapolating the linear portion of a stress–strain flow-curve to the stress axis) and the critical shear stress for erosion τ_s can be related as:

$$\begin{aligned} \tau_s &= 0.256\ \tau_y \quad \text{for} \quad \tau_y > 1.27\ Pa, \\ \tau_s &= 0.289\ \tau_y^{1/2} \quad \text{for} \quad \tau_y \leq 1.27\ Pa. \end{aligned} \tag{3}$$

This relationship is applied here as it is based on viscometric data from a wide range of marine muds and some fine powders. Based on the observations, the beginning of the bed erosion period suggests a critical shear stress for erosion

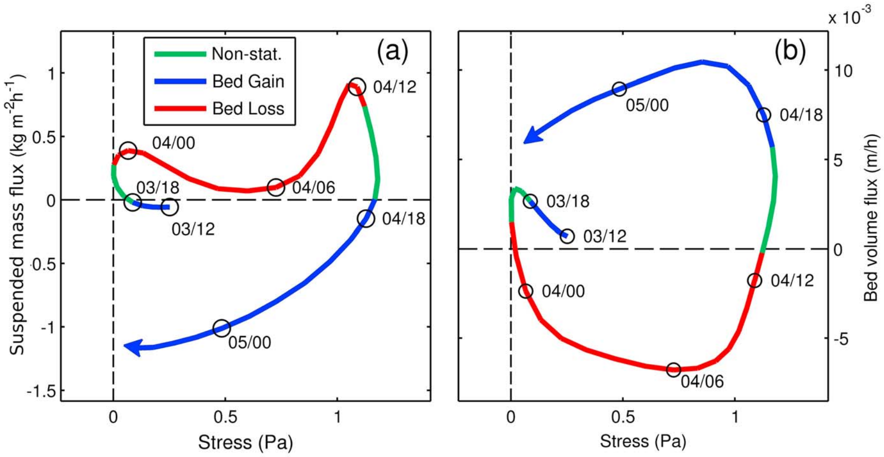

Figure 6. (a) Observed mass (water column) flux and (b) volume (bed) flux, versus numerically computed bed stress. The hysteresis showing curves are parameterized by time, with arrows pointing to the direction of time axis. Colors mark time intervals identified as dominated by bed/water column mass exchange (red: bed loss, blue: bed gain) or by lateral flux convergence (green: advective gain). Note that the first non-stationary time interval indicated with green is due to bed dilation.

$0.3\ \mathrm{Pa} \leq \tau_s \leq 0.5\ \mathrm{Pa}$, which corresponds to a yield stress of $1.1\ \mathrm{Pa} \leq \tau_y \leq 1.95\ \mathrm{Pa}$ (equation (3)).

[32] These values permit a back-estimation of the bed density and floc size at the onset of erosion. The corresponding volume fraction for solids of $0.075 \leq \phi_{vs} \leq 0.085$ (equation (B2), see also Figure B1), yields a bed density of $1{,}145\ \mathrm{kg/m^3} \leq \rho_{bed} \leq 1{,}160\ \mathrm{kg/m^3}$ (equation (B1)), with a floc size range of between 175 μm and 205 μm [*Safak et al.*, 2010, equation (4)]. These values agree with the laboratory tests [*Robillard*, 2009] (Appendix B), as well as with the 2006 LISST particle size observations given in *Safak et al.* [2010].

4.2. Mass Balance Considerations

[33] For conditions where the amount of suspended sediment is controlled by the vertical fluxes and sediment exchange with the bed, previous studies [e.g., *Letter and Mehta*, 2011] suggest that under a constant turbulent stress applied to the bed, the suspended-sediment mass approaches an equilibrium value at which the deposition and erosion fluxes practically balance out provided the entire cohesive sediment size range present is included in the analysis. Dampening of turbulence by the suspended sediment, and the fact that the yield stress as well as the critical shear stress for erosion increase with depth in the stratified bed as sediment is removed, are factors that may accelerate the realization of a near-equilibrium state in the field.

[34] The net sediment mass flux calculated as $\frac{d}{dt}\int_D SSC(z)dz$, where $SSC(z)$ is the estimated vertical SSC profile (Figure 5b) and D is the model domain (approximately the first mab), is plotted in Figure 6a against the computed bottom stress (Figure 5d). Here, concentrations above the PC-ADP range were not taken into account as the SSC in the upper column is negligible compared to that in the first mab. There is some positive mass flux between March 3rd at 18:00 hours and March 4th 03:00 hours when the bottom stress is less than 0.3 Pa which is likely related to the entrainment of soft bed. The net flux increases significantly with increasing bottom stress only after March 4th 04:00 hours, when the bed stress $\tau \simeq 0.5$ Pa is in the range of the critical shear stress for erosion (see section 4.1). The net flux reaches a maximum on March 4th at 12:00 hours when the seabed reaches its lowest position (Figure 4). The net flux cancels, i.e., deposition balances erosion, as the bed stress reaches its maximum value; then the cycle reverses, with the water column losing suspended sediment mass by deposition and the stress decreasing during the waning phase of the storm.

[35] Figure 6b shows the relation between the evolution of the computed bed stress and the net bed-volume flux $-\frac{dh}{dt}$, where $z = h(t)$ is the bed position (Figure 4c). The sign insures that positive fluxes raise the bed position (add sediment to the bed). The dependency is consistent with expectations, with erosion occurring as the stress increases and accretion as the stress decreases.

[36] The fact that the two curves in Figure 6 have different shapes is significant. The bed accreting when the sediment mass in the water column is still increasing (with decreasing rate) from March 4th at 12:00 hours to 18:00 hours which is a clear indicator of the sediment import through advection. Under the assumption that the mass fluxes are strictly vertical and the only source of sediment is the bed (known to be incorrect during the water front passage), the transfer function that maps the two panels of Figure 6 onto each other is the bed density. The shapes would be identical (with signs reversed), if the density of the mobilized layers was constant. The different shapes, therefore, offer some insight into the likely variability in the density of the mobilized bed layers.

[37] However, the physical interpretation of Figure 6 is not trivial. First, the curves use computed bed stresses that are not realistic everywhere; for example, the stress is likely overestimated during water front passage. Second, the density estimate derived by taking the ratio of the two curves has zeros when the numerator (water column flux) is zero and singularities when the denominator (bed-volume flux) is

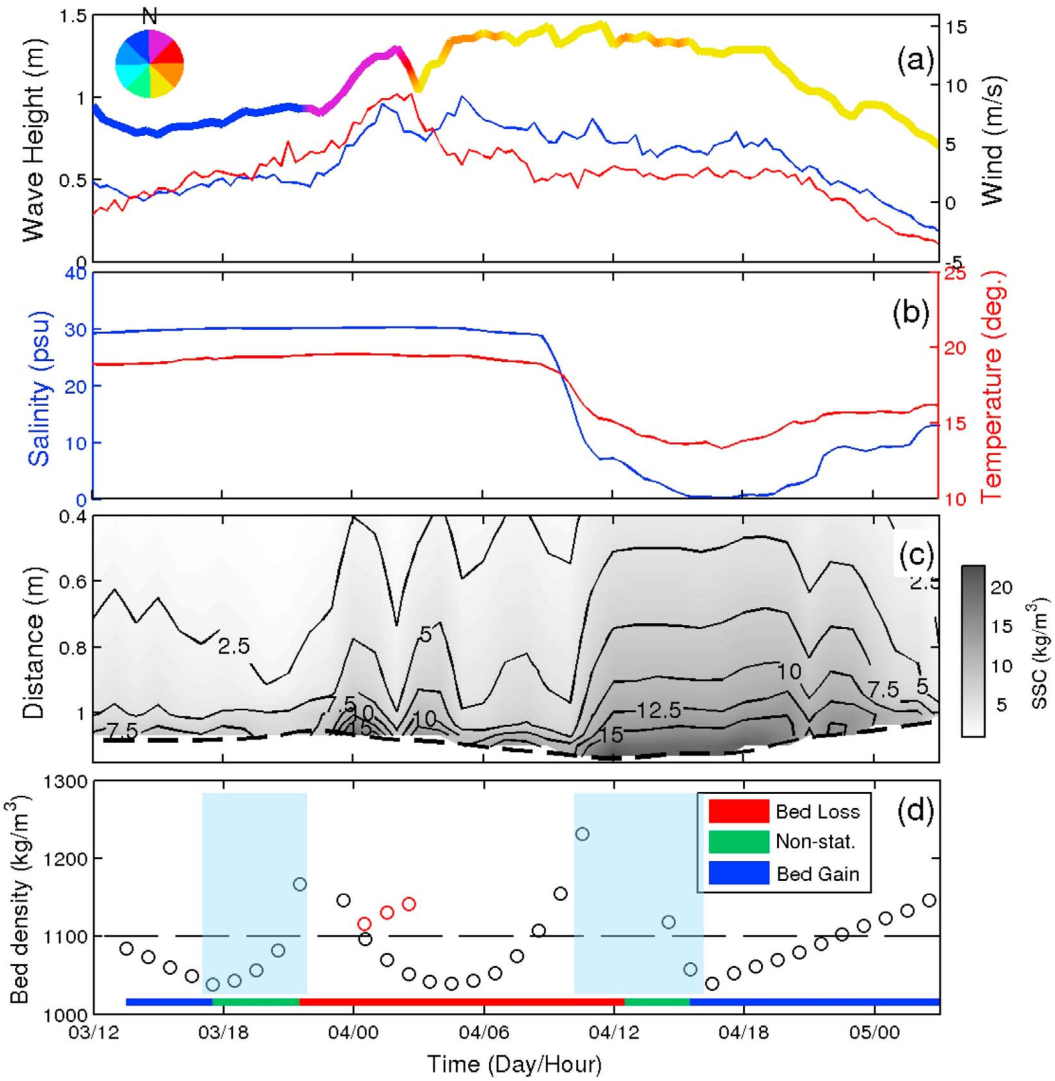

Figure 7. A summary of the bed reworking cycle during the storm of March 3rd to 5th, 2008. (a) Wind speed and direction, and significant wave heights (short-wave: blue and swell: red). (b) Salinity (blue) and temperature (red) at 55 cmab (c) Vertical profile of SSC estimated based on the PC-ADP backscatter. (d) Density of the removed/deposited bed layers estimated directly as the ratio of the mass/volume fluxes (Figure 6). In Figure 7d, the red circles mark the density values independently estimated from the observed yield stress range. The dashed line marks the gelation density for Atchafalaya mud [*Robillard*, 2009]. Blue rectangles cover the periods where the numerical model used in this analysis is likely invalid.

zero. These points have to be discarded. If mass exchange were strictly between the water column and the bed, the numerator and the denominator would cancel simultaneously. This is clearly not the case; the zero of the water column flux lags the zero of the bed flux by approximately 6 hours during the frontal passage between March 4th 12:00–18:00 hours, the time lag between two fluxes is about two hours during the bed dilation period between March 3rd 18:00 hours and March 4th 00:00 hours. Finally, the basic assumption of vertical fluxes and mass exchange strictly between the bed and the water column can be expected to be invalid during the non-stationary bed dilation time segment and the passage of the sediment laden front.

[38] A simple examination of the signs of the fluxes can help exclude the advection-dominated cases. If the two fluxes have the same sign, both the water column and the bed gain/lose mass at the same time, which is a clear indication of horizontal sediment-flux convergence, i.e., the horizontal gradient of SSC becomes important due to sediment advection (opposite signs only mean that the contribution of advection is not clear) during the passage of sediment laden front. This definition excludes the time segment between March 3rd 18:00 hours and March 4th 00:00 hours. Both fluxes have the same sign during this period, but the reason of bed level rise when sediment flux is increasing is due to bed dilation rather than sediment

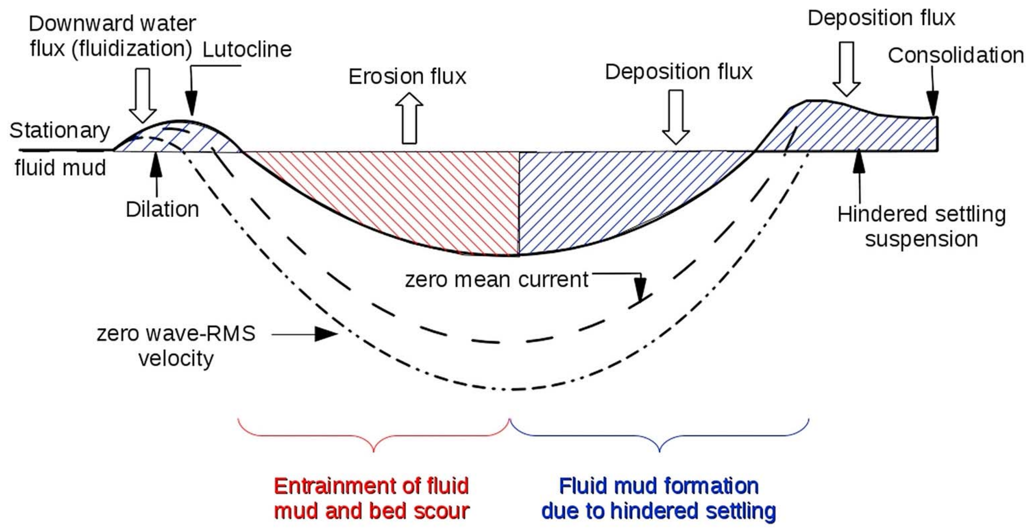

Figure 8. Idealized sketch of bed reworking during the storm.

deposition. The result of this check is marked with different colors in Figure 6, and largely agrees with the proposed interpretation. Note that as expected the dilation and advection-dominated green regions span the time interval between the zeros of the two fluxes.

5. Summary

[39] A summary of the results is shown in Figure 7. The storm was caused by the passage of a cold atmospheric front. Its duration was approximately 2 days; winds (and short waves) changed from southerly to northerly when the front passed over the observation site (Figure 7a); the mean current was dominated by the storm-generated weak surge and the subsequent flushing of the bay; halfway through the storm, the site was impacted by a sediment-laden fresh water plume from the Atchafalaya River mouth (Figures 7b and 7c). These features are characteristic to frontal passages, but as such they are expected to be a defining part of wave-sediment interaction during these storms.

[40] Figure 8 shows an idealized sketch of bed state evolution during the storm. In the absence of direct observations of bed states, we analyzed the hydrodynamic manifestation of bed reworking. Together with the acoustic backscatter intensity, the vertical profile of flow velocity (mean and variance) provides important clues on the location and the motion of the bed, and suggest a sequences of stages that could be described as: 1) fluidization/dilation, 2) erosion; 3) deposition/accretion; 4) fluid mud formation; 5) consolidation. At the peak of activity, a surficial layer of the bed of about 20–30 cm thickness oscillates with the waves (velocities 10–20 cm/s) and slides downslope at 5–10 cm/s.

[41] The 1DV model of *Hsu et al.* [2009] is used to investigate those processes that could not be observed directly. The model seeks an equilibrium state for the hydrodynamic/sedimentary system based on mass exchange between the bed and the water column. We are able to tune the model with both hydrodynamic data (mean and oscillatory flows) and sediment data (vertical profiles of SSC, Figure 7c). The model performs poorly during notably non-stationary conditions (e.g., bed dilation) and is likely invalid during the passage of the water front. However, the natural spatial uniformity of the site and conditions suggest that the numerical simulations are reliable – outside the brief period of water-front passage and a bed dilation event involving low sediment concentrations (blue rectangles in Figure 7d). Based on the goodness of the overall performance of the model, the simulations are used to gain insight into the bed reworking processes.

[42] Within the domain of validity of the model, the assumption that sediment mass balance is dominated by vertical exchange between the water column and bed permits a rough estimation of the density of the bed layers eroded/deposited during the storm (Figure 7d). The values indicate a softening of the bed under wave action in early stages of erosion, and increase in density after March 04th 04:00 hours since the bed layers become stiffer (critical shear stress is also increasing) with depth. The bed density likely decreases with start of deposition on March 4th 12:00 hours due to accumulation of soft mud on the bed (note that the values in Figure 7d are likely invalid during this period) and a steady increase in density starting with hindered settling, past the gelling point during consolidation based on the measured characteristic values of Atchafalaya mud at the gelling point (ρ_{Gel} = 1100 kg/m^3 [*Robillard*, 2009; *Sheremet et al.*, 2011], Figure 7d). The bed density at the onset of erosion and values independently estimated from the observed yield stress range (red circles in Figure 7d) are remarkably close, the values are also consistent with the fluid mud density range, 1050 kg/m^3–1200 kg/m^3 [*Jain and Mehta*, 2009]. Calculated near-bed shear stresses suggest a value for the critical stress for erosion in the range of 0.3 Pa to 0.5 Pa.

[43] The observations, laboratory tests and numerical simulations are consistent, and the results are probably to a certain degree universal, with the possible exception of the features that are specific to frontal passages (e.g., fresh water fronts). However, it should be stressed that a definitive

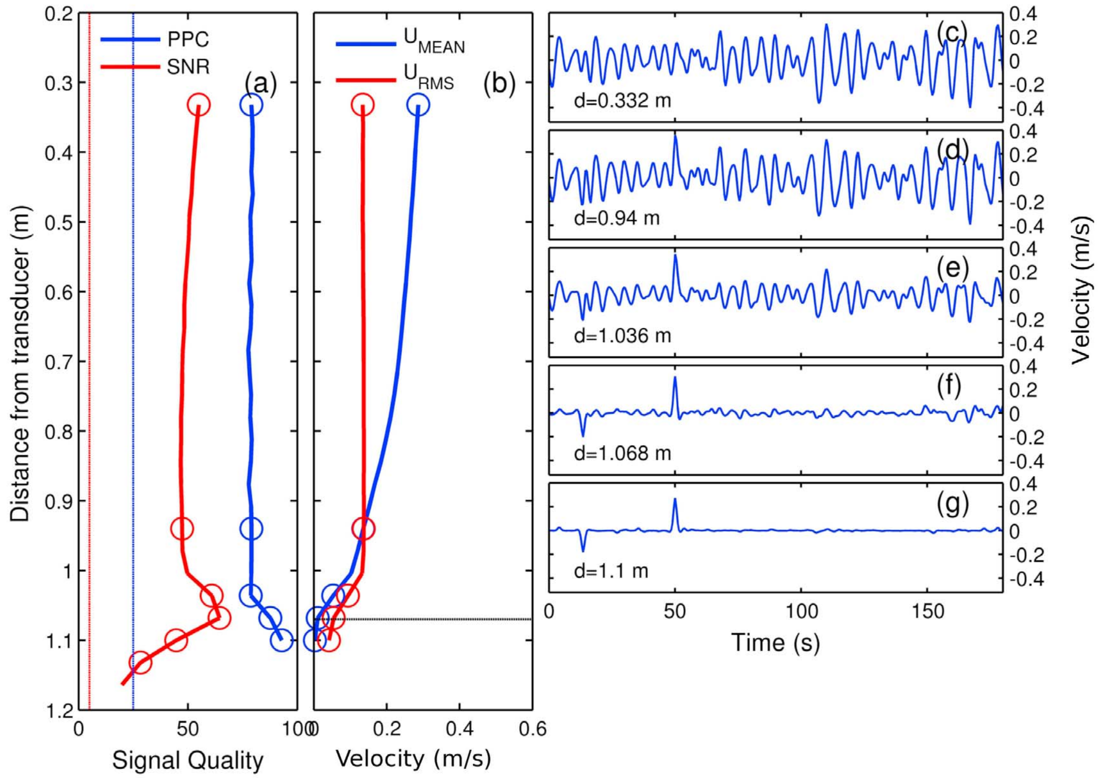

Figure A1. Sample of PC-ADP observations on March 3rd, 13:00 hours, during a period when the bed can be considered as stationary. (a) Ping-to-ping correlation (blue) and signal-to-noise ratio (red). Vertical lines mark the recommended acceptable-value threshold; circles mark the location of the bins plotted on the right. (b) Profiles (20-min averages) of the mean and RMS velocity. (c–g) Sample velocity time series at the bin locations marked in Figures A1a and A1b.

validation is not possible without direct observations of the bed state (difficult, and so far unavailable). Future efforts should focus on obtaining such observations as well as validation of the bed reworking dynamics inferred here.

Appendix A: Vertical Structure of Flow

[44] Two 3-min samples of the vertical structure of the flow velocity are shown in Figures A1 and A2. The samples are representative of: 1) pre-storm conditions on March 3rd at 13:00 hours (Figure A1 - compare with the position of the bed in Figure 4c), and 2) bed-mobilization conditions attained when the water front passed over the site on March 4th, 12:00 hours. The data are relatively noisy, but the waveforms recorded are consistent at all the measurements bins, and standard measures of quality (ping-to-ping correlation and signal-to-noise ratio) throughout the profiling range are within the recommended values given by the manufacturer. The variances may be slightly overestimated due to occasional spikes introduced by the algorithm for velocity ambiguity removal. The location of ZMV and ZRV were estimated by logarithmic extension of the two data points with reliable data closest to the bed.

[45] Pre-storm conditions are characterized by a clear cut-off depth for horizontal motion (Figure A1b). In contrast, bed-mobilization conditions in Figure A2b suggest that wave motion penetrated well below the estimated bed position.

Appendix B: Yield-Stress Measurements

[46] The range for the critical shear stress for erosion suggested by observations (0.3 Pa< τ_s <0.5 Pa) is consistent with the results from laboratory tests of *Robillard* [2009] conducted on samples from the experimental site. Here, we use the strain-stress flow-curve obtained by *Robillard* [2009] from rheometric oscillatory tests (10-s period) for solids volume fractions 0.0543< ϕ_{vs} <0.214 and simulated pre- and post-storm conditions (corresponding to high and low shear stress initial condition, respectively). The solids volume fraction is defined as

$$\phi_{vs} = \frac{\rho_f - \rho_w}{\rho_s - \rho_w}. \tag{B1}$$

where ρ_f, ρ_w and ρ_s are densities of mud flocs, water and primary sediment particles. Upper-Bingham yield-stress values were estimated as strain-axis intercept [*Barnes*, 1999]. The results (Table B1) show little variation between pre- and post-storm conditions.

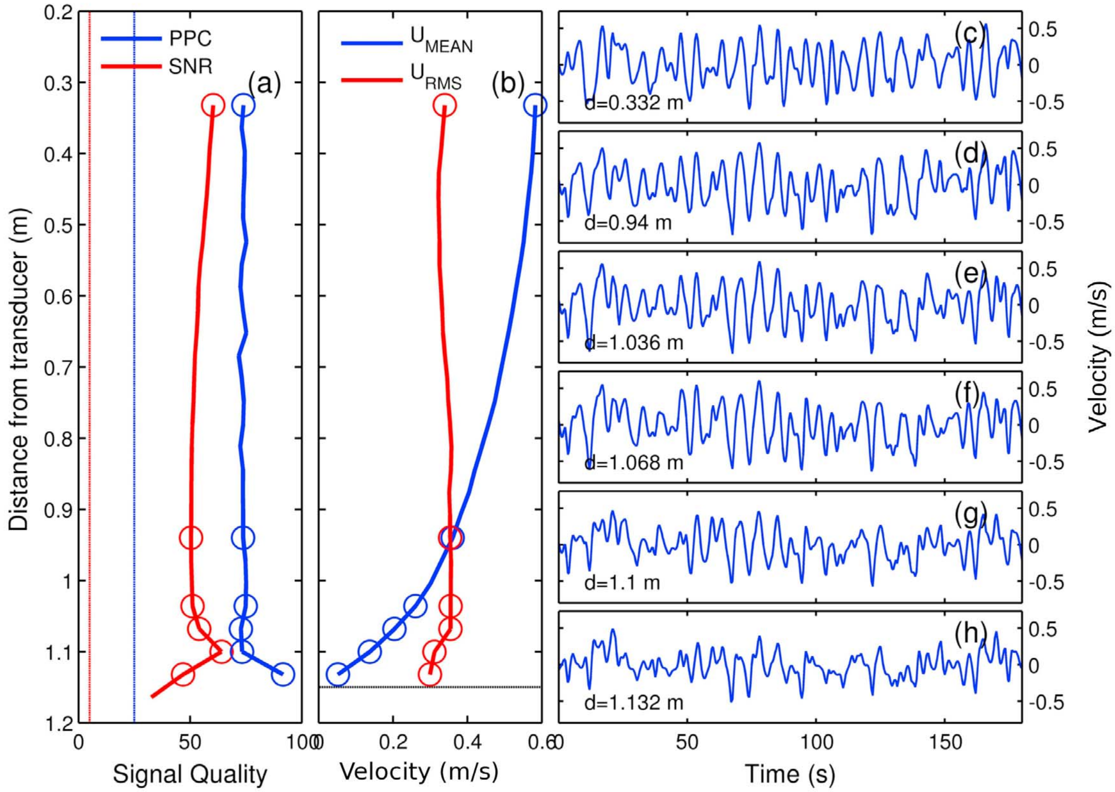

Figure A2. Sample of PC-ADP observations on March 4th, 12:00 hours UTM, at the maximum erosional depth (Figure 4c). (a) Ping-to-ping correlation and signal-to-noise ratio. (b) Profiles (20-min averages) of the mean and RMS velocity. (c–h) Sample velocity time series at bin locations marked by circles in Figures A2a and A2b.

[47] Above the space-filling (or gelation) concentration, the relationship between the yield stress τ_y and solids volume fraction follows the law [*Buscall et al.*, 1988]

$$\tau_y \sim \phi_{vs}^n. \tag{B2}$$

with n=4 $\pm$ 0.5. For the Atchafalaya mud, the values in Table B1 yield

$$\tau_y = 10^{4.53}\phi_{vs}^4. \tag{B3}$$

The dependency in equation (B3) is compared in Figure B1 to measurements for different marine sediments from Europe and Africa [*Migniot*, 1968]. The behavior of the Atchafalaya mud follows a similar trend with the other sediments with a slightly smaller slope. The difference in the slopes likely stems from different measurement techniques used, as *Migniot*'s [1968] results are based on rotational viscometer measurements while *Robillard* [2009], for Atchafalaya mud, used oscillatory test in a controlled-stress rheometer

Table B1. Yield Stress Estimates for Different Sediment Volume Fractions

Solids Volume Fraction	Yield Stress (Pre-storm) (Pa)	Yield Stress (Post-storm) (Pa)
0.0543	0.30	0.38
0.125	6.24	6.46
0.214	89.84	82.00

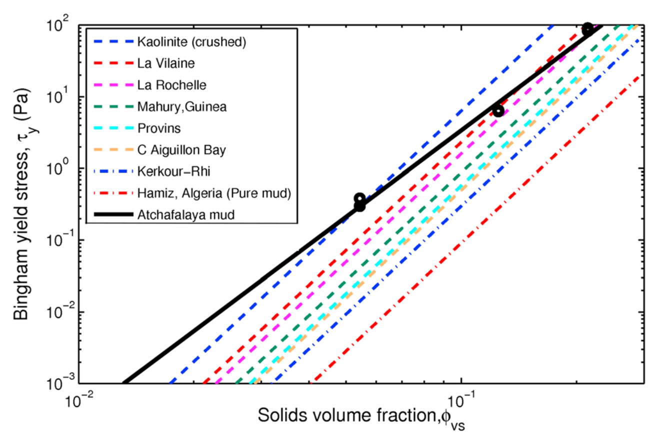

Figure B1. Upper-Bingham yield stress as a function of the solids volume fraction for different types of sediment (adapted from *Migniot* [1968]). Atchafalaya mud estimates are marked by black circles.

(AR2000ex) which can provide highly accurate stress-strain rate resolutions.

[48] **Acknowledgments.** This research was supported by the Office of Naval Research funding of contracts N00014-10-1-0363, N00014-10-1-0805, and N00014-11-1-0269. The corresponding author acknowledges the Council of Higher Education, Turkey and the Yildiz Technical University for the scholarship offered during his doctoral study. We are grateful to T.-J. Hsu for providing the numerical model for simulations. Sergio Jaramillo, Uriah M. Gravois and the field support group of Coastal Engineering Laboratory of University of Florida helped in the deployment and retrieval of the instruments. We thank the two anonymous reviewers for suggestions that improved the manuscript.

References

Allison, M. A., G. C. Kineke, E. S. Gordon, and M. A. Goni (2000), Development and reworking of a seasonal flood deposit on the inner continental shelf off the Atchafalaya River, *Cont. Shelf Res.*, *20*, 2267–2294.

Allison, M. A., A. Sheremet, M. A. Goni, and G. W. Stone (2005), Storm layer deposition on the Mississippi-Atchafalaya subaqueous delta generated by Hurricane Lili in 2002, *Cont. Shelf Res.*, *25*, 2213–2232.

Barnes, H. A. (1999), The yield stress—A review or '$\pi\alpha\nu\tau\alpha\ \rho\epsilon\iota$'—Everything flows?, *J. Non-Newtonian Fluid Mech.*, *81*, 133–178.

Buscall, R., P. D. A. Mills, J. W. Goodwin, and D. W. Lawson (1988), Scaling behavior of the rheology of aggregate networks formed from colloidal particles, *J. Chem. Soc. Faraday Trans. 1, 84*(12), 4249–4260.

Cacchione, D. A., D. E. Drake, R. W. Kayen, R. W. Sternberg, G. C. Kineke, and G. B. Tate (1995), Measurements in the bottom boundary layer on the Amazon subaqueous delta, *Mar. Geol.*, *125*, 235–257.

Chan, I.-C., and P. L.-F. Liu (2009), Responses of Bingham-plastic muddy seabed to a surface solitary wave, *J. Fluid Mech.*, *618*, 155–180.

Dalrymple, R. A., and P. L.-F. Liu (1978), Waves over soft muds: A two-layer fluid model, *J. Phys. Oceanogr.*, *8*, 1121–1131.

Draut, A. E., G. C. Kineke, D. W. Velasco, M. A. Allison, and R. J. Prime (2005), Influence of the Atchafalaya River on recent evolution of the chenier-plain inner continental shelf, northern Gulf of Mexico, *Cont. Shelf Res.*, *25*, 91–112.

Foda, M. A., J. R. Hunt, and H.-T. Chou (1993), A nonlinear model for the fluidization of marine mud by waves, *J. Geophys. Res.*, *98*(C4), 7039–7047.

Gade, H. G. (1958), Effects of a non-rigid, impermeable bottom on plane surface waves in shallow water, *J. Mar. Res.*, *16*, 61–82.

Gartner, J. W. (2004), Estimating suspended solids concentrations from backscatter intensity measured by acoustic Doppler current profiler in San Francisco Bay, California, *Mar. Geol.*, *211*, 169–187.

Hoitink, A. J. F., and P. Hoekstra (2005), Observations of suspended sediment from ADCP and OBS measurements in a mud-dominated environment, *Coastal Eng.*, *52*, 103–118.

Hsiao, S. V., and O. H. Shemdin (1980), Interaction of ocean waves with a soft bottom, *J. Phys. Oceanogr.*, *10*, 605–610.

Hsu, T.-J., P. A. Traykovski, and G. C. Kineke (2007), On modeling boundary layer and gravity-driven fluid mud transport, *J. Geophys. Res.*, *112*, C04011, doi:10.1029/2006JC003719.

Hsu, T.-J., C. E. Ozdemir, and P. A. Traykovski (2009), High-resolution numerical modeling of wave-supported gravity-driven mudflows, *J. Geophys. Res.*, *114*, C05014, doi:10.1029/2008JC005006.

Jain, M., and A. J. Mehta (2009), Role of basic rheological models in determination of wave attenuation over muddy seabeds, *Cont. Shelf Res.*, *29*, 642–651.

Jaramillo, S., A. Sheremet, M. A. Allison, A. T. Reed, and K. T. Holland (2009), Wave-mud interactions over the muddy Atchafalaya subaqueous clinoform, Louisiana, USA: Wave-driven sediment transport, *J. Geophys. Res.*, *114*, C04002, doi:10.1029/2008JC004821.

Jiang, F., and A. J. Mehta (1996), Mudbanks of the southwest coast of India. V: Wave attenuation, *J. Coastal Res.*, *12*(4), 890–897.

Jiang, F., and A. J. Mehta (2000), Lutocline behavior in high-concentration estuary, *J. Waterw. Port Coastal Ocean Eng.*, *126*(6), 324–328.

Kineke, G. C., E. E. Higgins, K. Hart, and D. Velasco (2006), Fine-sediment transport associated with cold-front passages on the shallow shelf, Gulf of Mexico, *Cont. Shelf Res.*, *26*, 2073–2091.

Letter, J. V., Jr., and A. J. Mehta (2011), A heuristic examination of cohesive sediment bed exchange in turbulent flows, *Coastal Eng.*, *58*, 779–789.

Liu, K.-F., and C.-C. Mei (1989), Approximate equations for the slow spreading of a thin sheet of Bingham plastic fluid, *Phys. Fluids A*, *2*, 30, doi:10.1063/1.857821.

Liu, K.-F., and C.-C. Mei (1993), Long waves in shallow water over a layer of Bingham-plastic fluid mud—I. Physical aspects, *Int. J. Eng. Sci.*, *31*(1), 125–144.

Lynch, J. F., T. F. Gross, B. H. Brumley, and R. A. Filyo (1991), Sediment concentration profiling in HEEBLE using a 1-MHz acoustic backscatter system, *Mar. Geol.*, *99*, 361–385.

Maa, J. P.-Y., and A. J. Mehta (1990), Soft mud response to water waves, *J. Waterw. Port Coastal Ocean Eng.*, *116*(5), 634–650.

Migniot, C. (1968), Etude des propriétés physiques de différents sediments très fins et de leur comportement sous des actions hydrodynamiques, *Houille Blanche*, *7*, 591–620.

Ng, C.-N. (2000), Water waves over a muddy bed: A two-layer Stokes boundary layer model, *Coastal Eng.*, *40*, 221–242.

Robillard, D. J. (2009), A laboratory investigation of mud seabed thickness contributing to wave attenuation, PhD dissertation, Univ. of Fla., Gainesville. [Available at http://purl.fcla.edu/fcla/etd/UFE0024823.]

Safak, I., A. Sheremet, M. A. Allison, and T. J. Hsu (2010), Bottom turbulence on the muddy Atchafalaya Shelf, Louisiana, USA, *J. Geophys. Res.*, *115*, C12019, doi:10.1029/2010JC006157.

Sahin, C., I. Safak, A. Sheremet, and M. A. Allison (2011), Bed-sediment response to energetic waves, Atchafalaya Inner Shelf, Louisiana, in *The Proceedings of Coastal Sediments 2011*, vol. 3, pp. 2415–2424, World Sci., Singapore.

Sheng, J., and A. E. Hay (1988), An examination of the spherical scatter approximation in aqueous suspensions of sand, *J. Acoust. Soc. Am.*, *83*, 598–610.

Sheremet, A., and G. W. Stone (2003), Observations of nearshore wave dissipation over muddy sea beds, *J. Geophys. Res.*, *108*(C11), 3357, doi:10.1029/2003JC001885.

Sheremet, A., A. J. Mehta, B. Liu, and G. W. Stone (2005), Wave-sediment interaction on a muddy inner shelf during Hurricane Claudette, *Estuarine Coastal Shelf Sci.*, *63*, 225–233.

Sheremet, A., S. Jaramillo, S.-F. Su, M. A. Allison, and K. T. Holland (2011), Wave-mud interactions over the muddy Atchafalaya subaqueous clinoform, Louisiana, United States: Wave processes, *J. Geophys. Res.*, *116*, C06005, doi:10.1029/2010JC006644.

Thorne, P. D., and D. M. Hanes (2002), A review of acoustic measurement of small-scale sediment processes, *Cont. Shelf Res.*, *22*, 603–632.

Thorne, P. D., P. J. Hardcastle, and R. L. Soulsby (1993), Analysis of acoustic measurements of suspended sediments, *J. Geophys. Res.*, *98*(C1), 899–910.

Thosteson, E. D., and D. M. Hanes (1998), A simplified method for determining sediment size and concentration from multiple frequency acoustic backscatter measurements, *J. Acoust. Soc. Am.*, *104*(2), 820–830.

Traykovski, P., W. R. Geyer, J. D. Irish, and J. F. Lynch (2000), The role of wave-induced density-driven fluid mud flows for cross-shelf transport on the Eel River continental shelf, *Cont. Shelf Res.*, *20*, 2113–2140.

Traykovski, P., P. L. Wiberg, and W. R. Geyer (2007), Observations and modeling of wave-supported sediment gravity flows on the Po prodelta and comparison to prior observations from the Eel shelf, *Cont. Shelf Res.*, *27*, 375–399.

Winterwerp, J. C., and W. G. M. van Kesteren (2004), *Introduction to the Physics of Cohesive Sediment in Marine Environment*, Elsevier, New York.

Winterwerp, J. C., R. F. de Graaff, J. Groeneweg, and A. P. Luijendijk (2007), Modeling of wave damping at Guyana mud coast, *Coastal Eng.*, *54*, 249–261.